The Astrophysical Journal, 945:37 (14pp), 2023 March 1 https://doi.org/10.3847/1538-4357/acb8bb

Role of Small-scale Impulsive Events in Heating the X-Ray Bright Points of the Quiet Sun

Biswajit Mondal[1,2], James A Klimchuk[3], Santosh V. Vadawale[1], Aveek Sarkar[1], Giulio Del Zanna[4], P. S. Athiray[5,6], N. P. S. Mithun[1], Helen E. Mason[4], and Anil Bhardwaj[1]
[1] Physical Research Laboratory, Navrangpura, Ahmedabad, Gujarat-380 009, India; biswajitm@prl.res.in, biswajit70mondal94@gmail.com
[2] Indian Institute of Technology Gandhinagar, Palaj, Gandhinagar, Gujarat-382 355, India
[3] NASA Goddard Space Flight Center, Heliophysics Science Division, Greenbelt, MD 20771, USA
[4] DAMTP, Centre for Mathematical Sciences, University of Cambridge, Wilberforce Road, Cambridge CB3 0WA, UK
[5] Center for Space Plasma and Aeronomic Research, The University of Alabama in Huntsville, Huntsville, AL 35899, USA
[6] NASA Marshall Space Flight Center, ST13, Huntsville, AL, USA
Received 2022 November 11; revised 2023 January 15; accepted 2023 January 29; published 2023 March 6

Abstract

Small-scale impulsive events, known as nanoflares, are thought to be one of the prime candidates that can keep the solar corona hot at its multimillion-Kelvin temperature. Individual nanoflares are difficult to detect with the current generation of instruments; however, their presence can be inferred through indirect techniques such as Differential Emission Measure (DEM) analysis. Here, we employ this technique to investigate the possibility of nanoflare heating of the quiet corona during the minimum of solar cycle 24. We estimate the DEM of disk-integrated quiet Sun and X-ray bright points (XBP) using the observations from XSM on board the Chandrayaan-2 orbiter and AIA on board the Solar Dynamic Observatory. XBPs are found to be the dominant contributor to disk-integrated X-rays, with a radiative flux of $\sim 2 \times 10^5$ erg cm^{-2} s^{-1}. XBPs consist of small-scale loops associated with bipolar magnetic fields. We simulate such XBP loops using the EBTEL hydrodynamic code. The lengths and magnetic field strengths of these loops are obtained through a potential field extrapolation of the photospheric magnetogram. Each loop is assumed to be heated by random nanoflares having an energy that depends on the loop properties. The composite nanoflare energy distribution for all the loops has a power-law slope close to -2.5. The simulation output is then used to obtain the integrated DEM. It agrees remarkably well with the observed DEM at temperatures above 1 MK, suggesting that the nanoflare distribution, as predicted by our model, can explain the XBP heating.

Unified Astronomy Thesaurus concepts: Solar coronal heating (1989); X-ray bright point (1812); Solar flares (1496); Solar coronal loops (1485); Solar x-ray emission (1536); Quiet solar corona (1992); Quiet sun (1322)

1. Introduction

Understanding the mechanism(s) that can heat the solar corona to several orders of magnitude hotter than its surface (≈6000 K) remains a long-standing problem in heliophysics. It is well-accepted that the magnetic field lines protruding out of the photosphere play a crucial role in heating the corona. The footpoints of the field lines are randomly moved by the convective motions below the photosphere, causing either the quasi-static buildup of magnetic stress or the generation of waves, depending on the timescale of the motion (Klimchuk 2006). Dissipation of magnetic stress is known as DC heating, whereas the dissipation of waves is known as AC heating. Most of the models of coronal heating, both DC and AC, suggest that the heating is impulsive in nature (Klimchuk 2006). Klimchuk (2015) defines the small-scale impulsive events as nanoflares, irrespective of the underlying physical mechanism. The magnitude and occurrence frequency of these nanoflares determine whether they can provide sufficient energy for the total heating.

Due to line-of-sight averaging and finite spatial resolution of the present generation of instruments, direct observation of individual nanoflares is difficult. Instead of their direct observable signature, several indirect methods are used to infer their existence, e.g., "Intensity Fluctuations" (Katsukawa & Tsuneta 2001; Pauluhn & Solanki 2007; Sakamoto et al. 2008), "Time Lags" (Viall & Klimchuk 2012, 2013, 2015; Bradshaw & Viall 2016), the "differential emission measure" (DEM), and the "emission measure distribution" (EMD). The DEM gives an estimation of the amount of plasma present at different temperatures (per unit temperature), and the integration of DEM over temperature bins provides the EMD.

The DEM technique has been extensively used in many observational studies to interpret the heating of quiescent active region cores in terms of heating frequencies (e.g., Tripathi et al. 2011; Winebarger et al. 2011; Brosius et al. 2014; Caspi et al. 2015; Del Zanna et al. 2015; Ishikawa et al. 2017). However, this technique has not been widely used to study the heating of the quiet solar corona. Earlier studies of the quiet Sun DEM (Lanzafame et al. 2005; Brooks et al. 2009; Del Zanna 2019) show a peak at low temperatures, around 1 MK. However, because of the faint emission at high temperatures (temperatures higher than 2MK), determining the quiet Sun DEM turns out to be difficult (Del Zanna & Mason 2018). Lately, using hard X-ray observations, Paterson et al. (2022) derived DEMs for different features of the quiet solar corona. They found faint emissions up to 4 MK. DEMs of the small-scale transient brightenings in the quiet solar corona have also been studied using EUV images (see, e.g., Berghmans et al. 2021; Chitta et al. 2021). The derived DEMs are seen to peak around 1–1.5 MK. While deriving DEMs of the coronal bright points, Chitta et al. (2013) found that they emit mostly around 2 MK before quickly fading away at high temperatures.

The X-ray quiet Sun has been studied using the Solar X-ray Monitor (XSM; Vadawale et al. 2014; Shanmugam et al. 2020) on board the Chandrayaan-2 orbiter during the minimum of solar cycle 24 (Vadawale et al. 2021b). They derived the isothermal temperature, emission measure, and elemental abundances of the quiet Sun. Comparing X-ray images of the Sun taken by the XRT/Hinode (Golub et al. 2007; Kosugi et al. 2007), they inferred that a large fraction (>50%) of the quiet solar X-ray emission arises from X-ray Bright Points (XBPs). XBPs are seen to be located all over the solar disk (Golub et al. 1974). It is, therefore, important to understand the contribution of XBPs to the total quiet solar emission and heating of the quiet corona. The quiet Sun includes quiet diffuse regions (QDRs), mostly emitting around 1 MK; cool coronal holes emitting at lower temperature (<1 MK); and X-ray emitting regions (XERs), the prime origin of the solar X-ray emissions, including limb brightening and the XBPs. One of the objectives of the present study is to quantify the contributions of XBPs and XERs to the total quiet Sun emission at different temperatures. For that, we derive the quiet Sun DEM by combining the observations in X-rays and EUV from the XSM and AIA. We have extracted the contribution of XERs and then XBPs from the total quiet Sun emission and estimated their DEM separately.

The second objective of this work is to study the role of impulsive events, so-called nanoflares, in maintaining the heating of XBPs. XBPs consist of small-scale rapidly evolving coronal loops (Madjarska 2019). Using the Enthalpy-Based Thermal Evolution of Loops (EBTEL; Klimchuk et al. 2008; Cargill et al. 2012, 2012) model, we simulate the XBP loops heated by nanoflares with different frequency distributions. The appropriate frequency distribution is determined using loop parameters derived from the extrapolated photospheric magnetograms. We derive a composite DEM for all the XBP loops and compare this with the observations to determine whether nanoflares could explain the heating of the XBPs.

The rest of the paper is organized as follows. In Section 2, the observation and the data analysis of the XSM and AIA are presented. In Section 3, the detailed method of the combined DEM analysis and results are described. Description of the XBPs simulation setup and results are given in Section 4. Finally, we discuss and summarize the primary findings of this work in Section 5.

2. Observations and Data Analysis

We use the X-ray observations of the Sun by XSM on board India's Chandrayaan-2 orbiter. XSM measures the disk-integrated solar spectra in the energy range of 1–15 keV at every second, with an energy resolution better than 180 eV at 5.9 keV (Shanmugam et al. 2020; Mithun et al. 2021). The unique design of XSM makes it possible to observe a wide range of solar X-ray intensities from the quiet Sun to X-class solar flares (Mithun et al. 2020). XSM started solar observations on 2019 September 12, and observed well the minimum of solar cycle 24 covering the years 2019 and 2020. During 2019 September to 2020 May, there were 76 days when no active regions (AR) were present on the solar disk (Vadawale et al. 2021b), defined as the Quiet Sun (QS) period. In the present study, two representative intervals are selected from the QS duration on 2019 September 20 (00:07 UTC–01:49 UTC, defined as QS-1) and 16 (20:00 UTC—22:00 UTC, defined as QS-2). Following the standard analysis procedures described in Vadawale et al. (2021b) and Mondal et al. (2021), we generate the XSM observed flux light curves in the energy range of 1–8 Å for the days that include QS-1 and QS-2, as shown in Figures 1(a) and (b). The orange shaded color marks the duration of QS-1 and QS-2.

The primary objective of the present study is to estimate the DEM/EMD for the QS period. Because XSM is more sensitive to higher temperatures (>2 MK), to constrain the DEM at lower temperatures (<2 MK), we need to combine XSM with EUV data (see Section 3). Thus, we combine the EUV observation from AIA (Lemen et al. 2012) on board SDO (Pesnell et al. 2012). AIA continuously records full-disk images of the Sun in different EUV energy channels (94 Å, 131 Å, 171 Å, 193 Å, 211 Å, 304 Å, and 355 Å) with a cadence of 12 s. During the QS-1 and QS-2 periods, the level-1 AIA full-disk images in all of its pass-bands were downloaded from Joint Science Operations Center (JSOC) and processed to level 1.5 using the standard routines available in the SolarSoftWare package (SSW; Freeland & Handy 1998). A representative full-disk image frame of the AIA 94 Å channel during the QS-1 period is shown in Figure 1(c).

3. Combined DEM Analysis

The DEM (or EMD) gives an indication of the amount of plasma that is emitting the radiation observed and has a temperature between T and $T + dT$ (Del Zanna & Mason 2018). To estimate the DEM, we use simultaneous observations, at several EUV and X-ray energy bands, sensitive to different temperatures. We use the five EUV channels of AIA, 94 Å, 131 Å, 171 Å, 193 Å, and 211 Å that are sensitive to temperatures over $\log T = 5.6$. We exclude the channel 335 Å due to a long-term drop in sensitivity resulting from accumulated contamination (Boerner et al. 2014; Athiray et al. 2020). For each AIA channel, we consider the integrated intensity of all the positive finite pixels below a solar radius of 1.04 $R_\odot$ (white circle in Figure 1(c)), where most of the emission is coming from in all the energies. We have verified that the final results remain unaffected even if we consider the pixels within a larger radius or even the full AIA field of view (FOV). For the X-ray observation, we divide the XSM spectrum into four energy channels of 1.29–1.45 keV, 1.45–1.75 keV, 1.72–1.95 keV, and 1.95–2.5 keV. These channels were chosen such that each includes a line complex of particular element/elements (Mg, Mg+Al, Si, and Si+S) with good statistics. Thus, we obtain the observed intensity in a total of nine instrument channels: five channels from AIA and four channels from XSM.

The observed intensity (O_i) at the ith instrument channel is related to the DEM as follows:

$$O_i = \int_T \mathrm{DEM}(T)\, R_i(T)\, dT + \delta O_i. \quad (1)$$

Here, δO_i is the uncertainty associated with O_i, and $R_i(T)$ is the temperature response function of the ith channel. The ability of an instrument channel to detect plasma emission at various temperatures is represented by its temperature response. Figure A1 shows the temperature response functions for AIA channels (dashed lines) along with the four XSM channels (solid lines). The detailed method to obtain the temperature response functions of XSM and AIA is described in Appendix A.

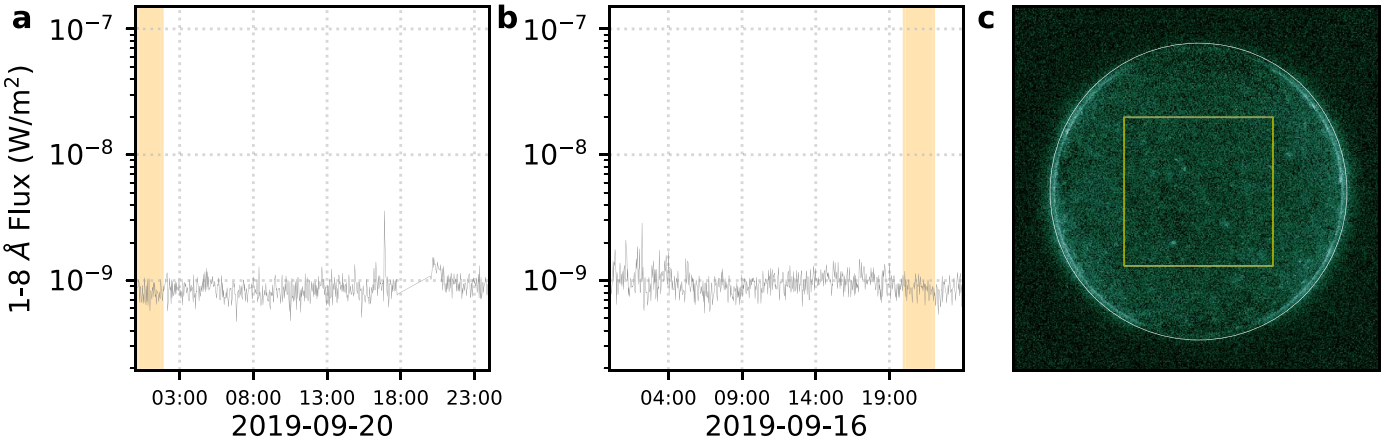

Figure 1. Panels (a) and (b) show the 1–8 Å light curve of the Sun observed by XSM during 2019 September 20 and 16. The orange shaded region represents the duration of QS-1 and QS-2 as mentioned in the text. Panel (c) shows a representative full-disk image of the Sun during QS-1 taken by AIA 94 Å channel. The yellow square box at the center shows a $1000'' \times 1000''$ field of view as mentioned in Section 3.3.

3.1. Full Sun DEM ($DEM_{FullSun}$)

The observed intensities (O_i) and temperature response functions of all the energy channels are already known. To recover the DEM, we use the `xrt_dem_iterative2.pro` (Golub et al. 2004) method (henceforth `xrt_dem`). This is basically a forward-fitting routine that finds the DEM solution from Equation (1) by considering a spline function for the DEM curve. This routine is a standard tool set for solar data analysis in the SolarSoftWare (SSW; Freeland & Handy 1998) package. The best-fit DEM is identified iteratively using a nonlinear least-squares method by comparing the predicted and observed fluxes. This method has been widely used in DEM fitting with AIA/SDO, XRT/Hinode, EIS/Hinode, and FOXSI data (e.g., Golub et al. 2007; Winebarger et al. 2011; Ishikawa et al. 2017; Wright et al. 2017; Athiray et al. 2020). Here, we consider a temperature range of $5.9 \leqslant \log T \leqslant 6.8$ with a bin size of $\delta \log T = 0.03$ for the DEM estimation. Monte Carlo (MC) runs are used to estimate the uncertainties in the recovered DEM. These runs are carried out by randomly changing the observed intensities within the observed errors. The errors in the AIA observed counts at each channel are estimated using the standard procedure, `aia_bp_estimate.pro` (Boerner et al. 2012). Uncertainties in the XSM observation primarily contain the Poisson error associated with the counting statistics and small systematic errors at each spectral channel provided by the XSM data processing software. To estimate the uncertainties in the recovered DEM solution, we perform a large set of (500,000) MC runs over the observed counts. Among all the MC samples, we ignore the spurious DEM solutions, e.g., selecting the DEM solutions that can describe the observed flux at all channels with a reduced chi-squared value less than or equal to 2. The histogram of the DEMs at each temperature node is derived using the accepted DEM solutions. From the peak of the DEM histogram at each temperature node, we estimate the one-sigma uncertainties.

The full Sun DEM (defined as $DEM_{FullSun}$) and the 1σ error bars are shown in Figure 2(a) for QS-1 (red) and QS-2 (blue). The solid line represents the peak of the DEM histogram at each temperature node. We derive the EMD (units of cm^{-3}) from the DEM (units of $cm^{-5}\ K^{-1}$) by multiplying the DEM by area $\times\ T\delta \log T$ (here, area is the total emitting area on the Sun and $\delta \log T$ is the logarithmic bin size of temperatures). The EMDs derived for QS-1 and QS-2 are shown in Figure 2(c). Dividing the observed counts with the temperature response function associated with each channel gives the emission-measure loci curves, which indicate the upper limit of the EMD. The emission-measure loci curves for the QS-1 (red curves) and QS-2 (blue curves) at the five AIA channels (left side) and four XSM channels (right side) are overplotted.

Here, we assume an integrated emission from the AIA images that includes the emission from the quiet region, XBPs, and the limb emission. However, from the full-disk X-ray images (e.g., XRT/Hinode Be-thin filter images) one can see that the X-ray emission from the quiet region is very very faint compared with the XBPs and limb emission. Thus, in the next step, we separate the X-ray Emitting Regions (XER) from the AIA full-disk images, as discussed in Section 3.2, and then combine the intensity of the XER from AIA images with the XSM observation to estimate the combined DEM of the XER, as discussed in Section 3.3.

3.2. Identification of XER in AIA EUV Images

In the full-disk X-ray and EUV images of the Sun, the XER are found to be bright compared with the surrounding quiet Sun emission. Thus, the XER emission can be separated out using a source detection technique. In this study, we have used the astronomical source detection algorithm, `Photutils` (Bradley et al. 2021), over the full-disk image of the AIA 193 Å channel in order to estimate the typical emitting regions of the XER. `Photutils` is a Python library that provides tools for detecting astronomical sources using image segmentation. The detected sources must have a minimum number of adjacent pixels, each of them greater than a given threshold value in an image. Usually, the threshold value is taken to be the background noise (sigma) multiplied by a factor. In our case, we have estimated the background noise of the quiet Sun emission in the AIA 193 Å images using the `detect_threshold` method of the `Photutils` and defined a threshold level of two times the background noise. We apply a 2D circular Gaussian kernel with a full width at half maximum (FWHM) of three pixels to smooth the image prior to applying the threshold. Using the `detect_sources` method of the Photutils, we find out all the distinct sources that have a minimum of five connected pixels. A mask frame of the same dimensions as the original image is prepared by assigning all the detected source pixels a value of one and the rest a value of zero. Multiplying the mask with the

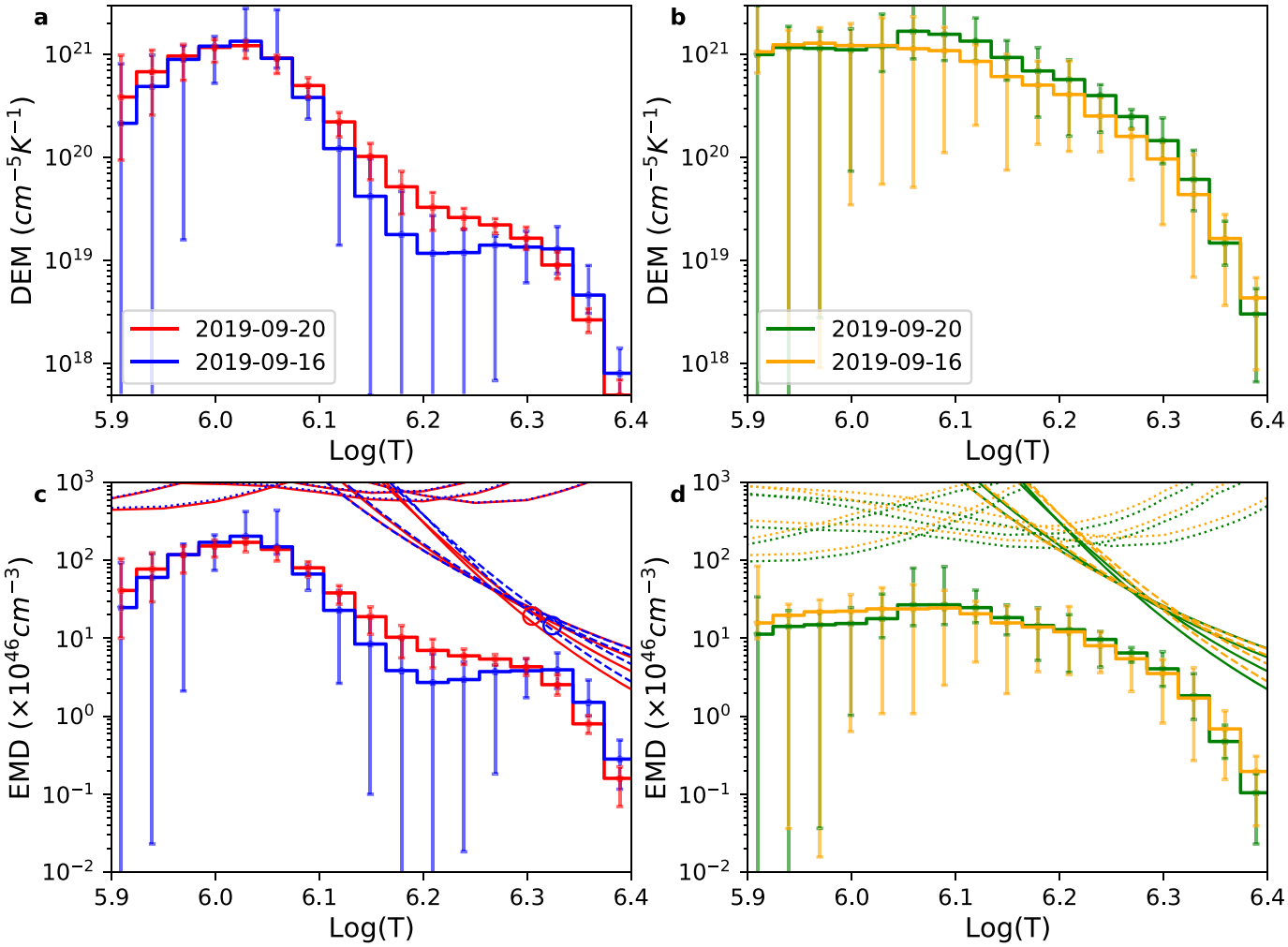

Figure 2. Panels (a) and (c) show the full Sun DEM and EMD profile for QS-1 (red) and QS-2 (blue). Panels (b) and (d) show the DEM and EMD for the XERs associated with QS-1 (green) and QS-2 (orange). The EM loci curves for AIA (dashed lines) and XSM (solid lines) are overplotted in panels (c) and (d). The red and blue circular points in Panel (c) represent the isothermal temperature and EM for the XER as reported by Vadawale et al. (2021b).

original image gives us a mask image, which provides the typical contribution of the XER. The same mask frame is used in all the AIA channels to find out the XER contribution in the respective passband.

Panels (a) and (d) in Figure 3 show a representative full-disk solar image and a zoomed-in view of the same image on 2019 September 20, taken in the AIA 193 Å channel. The bright regions represent the emission from XER. Panels (b) and (e) show the masked images of the original images (panels (a) and (d)). The masked images show a good agreement with the X-ray images taken by the XRT Be-Thin filter as shown in panels (c) and (f). The emission in the masked images (panels (b) and (e)) is well-matched with the X-ray images (panels (c) and (f)) except for a few places. The limb emission is not as noticeable in X-rays as it is at 193 Å, as we discuss later.

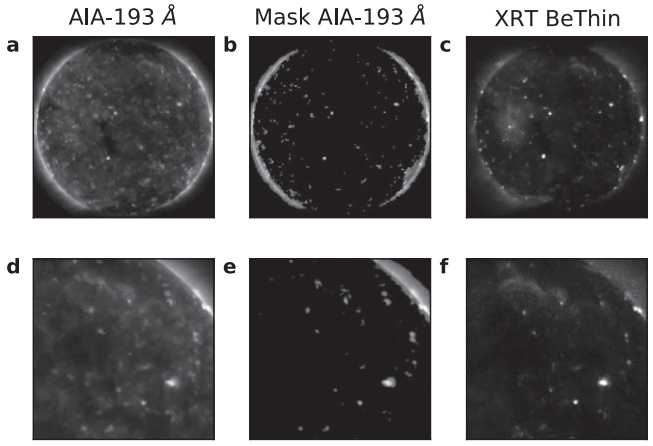

Figure 3. Full-disk images of the Sun during QS-1 taken by the AIA 193 Å channel (panel (a)) and XRT Be thin filter (panel (c)). Panel (b) shows the XERs extracted from the AIA 193 Å image. Panels shown in the bottom row represent a portion of the solar disk taken from the above panels.

3.3. DEM of XER (DEM_{XER})

Using the integrated emission from the XER in the AIA images (Section 3.2) along with the X-ray emission detected by XSM, we derive the DEM of X-ray emitting regions (henceforth DEM_{XER}) in a similar manner to the full Sun DEM (Section 3.1). Panels (b) and (d) of Figure 2 show the DEM and EMD of the XER during QS-1 (green) and QS-2 (orange). EM-loci curves for all AIA channels (left) and XSM channels (right) are also shown in panel (d). In the full Sun, as the emitting area for the high-temperature (>1.5 MK) emission is less than that of the cool plasma, the full Sun DEM (panel (a))

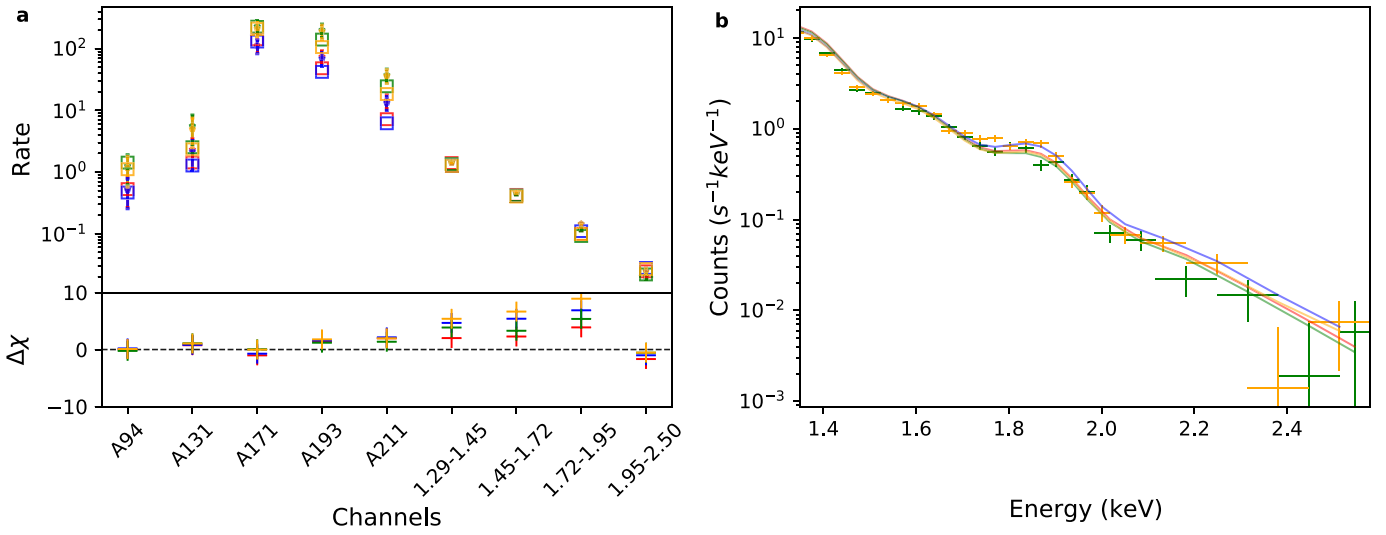

Figure 4. Panel (a) represents the observed intensities (in DN Px^{-1} s^{-1} for AIA and counts s^{-1} for XSM) of QS-1 and QS-2 measured in the different channels of AIA and XSM, and the square boxes represent the predicted intensities using the DEM shown in Figure 2. The panel underneath shows the delta-chi (i.e., (observed – predicted) / error) between the observed and predicted intensities. The error bars in panel (b) show the observed XSM spectra of QS-1 and QS-2. The solid lines shown in red, blue, green, and orange colors represent the XSM spectra predicted using the DEM shown in Figure 2.

at high temperatures is much lower than that of the XER (panel (b)). However, comparing the EMD of the full Sun (panel (c)) and that of the XER (panel (d)), we can say that the higher-temperature (>1.5 MK) portion is similar. This indicates that the hotter emission comes primarily from the XER. At lower temperatures, where the EMD is primarily determined by AIA, the full Sun EMD shows an excess emission.

3.4. Validation of Recovered DEMs

To verify the reliability of the recovered DEM/EMD as discussed in Sections 3.1 and 3.3, we estimate the predicted counts in all channels and the XSM spectra by using the recovered DEM and then compared them with the observed intensities and XSM spectra. The top panel of Figure 4(a) shows the observed (points with error bars) and predicted (box points) intensities (same color as Figure 2) in all the instrument channels using the DEM shown in Figure 2. The bottom panel indicates the delta-chi ((observed – predicted) / error) between the observed and predicted intensities, where the errors are the uncertainties in the observed intensities, δO_i, in Equation (1). The predicted intensities for all the recovered DEMs match the observed intensities to within the error bars.

Further, we forward-model the XSM spectra using the recovered EMD of both the full Sun (blue and red solid lines correspond to QS-1 and QS-2) and XER (orange and green solid lines correspond to QS-1 and QS-2), as shown by solid lines in Figure 4(b). For comparison, the observed XSM spectra during QS-1 (green error bars) and QS-2 (orange error bars) are overplotted. The modeled spectra derived from the EMD agree well with the observed ones. As XSM is most sensitive to higher temperatures, the excess emission at lower temperatures in the full Sun EMD (Figure 2(c)) does not contribute much to the modeled XSM spectra. Thus, the EMD from the full Sun and X-ray emitting regions explain the XSM spectra equally well. This verifies that most of the emission observed by XSM primarily originates from X-ray emitting regions.

3.5. DEM of XBPs (DEM_{XBP})

The DEM of the XER has contributions from both the XBPs and the limb brightening. Though the limb seems to be very bright in the full-disk images (Figure 3; specifically in AIA energy bands), it is well-known that the limb emission primarily comes from cool plasma with great line-of-sight depth. Thus, it is expected that the limb emission contributes mostly to the lower-temperature part of the DEM, whereas the high-temperature part comes primarily from the XBPs. However, in our recovered DEM, we found that at lower temperatures the error bars are very large, and we could not predict the DEM at very low temperatures, e.g., $\log T < 5.9$. This is due to the fact that, at those temperatures, the emissions are very faint and hence noisy; reliable results could not be recovered by the `xrt_dem` method. This uncertainty has been demonstrated nicely by Hannah & Kontar (2012) for a set of simulated data of the AR and quiet Sun for different AIA channels. Using a regularized inversion to solve Equation (1), Hannah & Kontar (2012) gave a different approach to estimate the DEM from the observed intensity of different instrument channels. The major advantage of this method is that it determines the errors of estimated DEM along with the uncertainty in temperature intervals. In the next step, we apply the Hannah & Kontar (2012) method[7] (henceforth `HK_dem`) to recover the DEM and compare the obtained DEM with that obtained by the `xrt_dem` method.

Using the `HK_dem` method, we have recovered the DEM_{XER} of QS-1 down to a lower temperature ($\log(T) = 5.6$). Figure 5(a) shows the DEMs derived by both the `HK_dem` and `xrt_dem` methods. Both the methods provide very similar results at higher temperatures (>1 MK). The `HK_dem` provides the DEM at lower temperatures with very large errors in the log (T) resolution, which could result in an underestimation of the lower-temperature DEM in a way similar to that demonstrated by Hannah & Kontar (2012).

To recover the DEM solely contributed by XBPs, we choose to derive DEM of the XBPs located within a square area of size

[7] https://github.com/ianan/demreg/tree/master/python

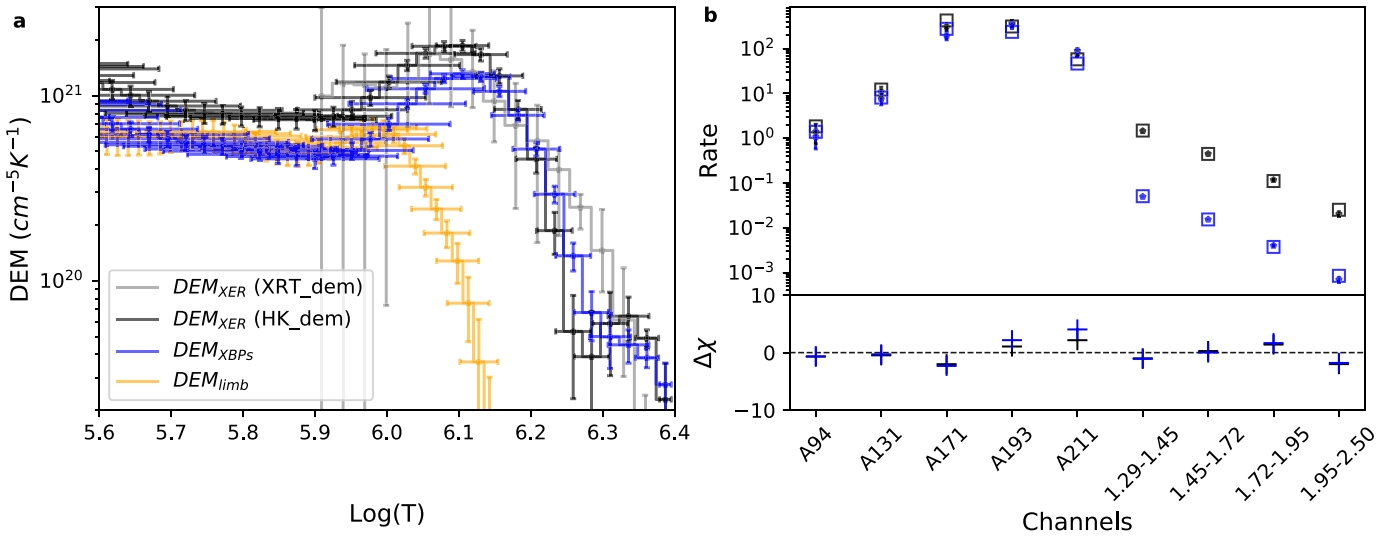

Figure 5. Panel (a) shows the observed DEMs of XER (black), XBPs (blue), and limb (orange) derived by HK_dem method. The DEM of XER derived by XRT_{dem} method is overplotted by gray shading. Panel (b) shows the observed (error bars) and predicted counts in different instrument channels.

$1000'' \times 1000''$, denoted as F_v, at the center of the solar disk. Such an area is marked with the yellow box in Figure 1(c). However, XSM provides an integrated count of the whole Sun, and the count from said box will only be a fraction (denoted f) of it. Earlier, we mentioned that the contribution of the quiet Sun emission is negligible compared to the emission from the XBPs. It is, therefore, safe to assume that XBPs are the primary contributor to the X-ray emission in the said box. To recover the DEM of the XBPs lying within this box, we first count the total number of visible XBPs within the box. We also count the total number of XBPs present on the whole disk. It is expected that reducing the XSM count using this number ratio may provide the count contribution from the box. However, it turns out that the X-ray limb emission affects the overall XSM count and introduces extra emission in the derived DEM. As a corrective measure, next we calculate the total area of all visible XBPs within the box and that of the XERs of the global Sun. If this area ratio is now used to reduce the XSM count and we subsequently use the reduced count to derive the DEM of the XBPs present within the box (DEM_{XBP}), we arrive at a reasonable solution. Blue error bars in Figure 5(a) show the estimated DEM_{XBP}, which predicts the observed intensities quite well (Figure 5(b)). Toward lower temperatures (<1 MK), DEM_{XBP} differs from the total XERs' DEM, which is quite expected, as at lower temperatures, limb emission also contributes to the total DEM.

A more sophisticated verification of contribution of limb emission to the total is done by estimating the typical DEM of the limb (DEM_{limb}) emission using different channels of AIA along with the XRT filter images. We select a small portion of the limb and then estimate the counts in AIA EUV channels along with the XRT `Al-mesh`, `Al-poly`, and `Be-thin` filters. Using a 20% uncertainty with the observed intensity along with a calibration factor of 2 (Athiray et al. 2020) for XRT, we estimated the DEM_{limb}. The recovered DEM for the limb is shown in orange color in Figure 5. This also indicates that the limb is only contributing emission at a lower temperature.

It should be noted that, at temperatures below 1 MK, there may be some uncertainty in determination of f, and hence in DEM_{XBP}. However, at temperatures above 1 MK, the estimated DEM_{XBP} is quite robust, as the contribution of the limb emission at these temperature is negligible. Thus, it can be safely assumed that the DEM_{XBP} shown in Figure 5 represents the average DEM for the XBPs.

4. Hydrodynamic Simulations of XBPs Emission

To investigate the energy requirement for XBPs to maintain the observed DEM (DEM_{XBP}), we carry out hydrodynamic simulations. XBPs are found to be associated with bipolar magnetic field regions, similar to active regions, and consist of independent, rapidly evolving small-scale loops (Madjarska 2019). It is thus natural to assume that the hot emission of XBPs is associated with the plasma confined within the small-scale magnetic loop systems, termed a magnetic skeleton. Field-aligned hydrodynamic models are often used to estimate the evolution of the plasma confined within the coronal loops. One such model is Enthalpy-Based Thermal Evolution of Loops (EBTEL; Klimchuk et al. 2008; Cargill et al. 2012, 2012). EBTEL is a zero-dimensional (0D) time-dependent hydrodynamic model that can accurately estimate the time evolution of the spatially averaged coronal temperature, density, and pressure of a single coronal loop heated by an assumed heating profile (time-dependent heating rate). The primary advantage of using 0D models such as EBTEL for such simulations is that their run time is orders of magnitude faster than that of spatially resolved 1D models. Despite the simplicity of the EBTEL calculation, it can provide plasma parameters very similar to the loop-averaged values from 1D models. Along with the average coronal properties of the loop, EBTEL estimates the DEMs of the transition region and coronal portion of the loop separately at each time step. Chitta et al. (2013) used EBTEL to simulate the emission of a coronal bright point, which had a morphology similar to that of an XBP. They assumed a heating profile for the fixed loop lengths of constant and varying cross sections. In this work, we have used the two-fluid version of EBTEL (EBTEL[8]++; Barnes et al. 2016, 2016), where the ions and electrons are treated separately; a detailed implementation of it can be found in Barnes et al. (2016).

Using the high-resolution full-disk photospheric magnetic field measurements from the Helioseismic and Magnetic

[8] https://rice-solar-physics.github.io/ebtelPlusPlus/

Imager (HMI; Scherrer et al. 2012) on board the SDO, we have extrapolated the magnetic field lines and produced the magnetic skeletons associated with the XBPs as discussed in Section 4.1; these provide the lengths and magnetic field strengths of the loops that comprise the skeleton. The loops are simulated with EBTEL using heating profiles that depend on the length and field strength as described in Section 4.2. The approach is similar to that used by Nita et al. (2018) for active regions.

4.1. Magnetic Skeleton of XBPs

We are interested in modeling all the XBPs emissions near the disk center within an area of $1000'' \times 1000''$ (defined as F_v in Section 3.5). Using the locations of all the XBPs within F_v (Section 3.2), we identified their respective counterparts on the full-disk line-of-sight (LOS) HMI magnetogram and find that all of them are associated with magnetic bipolar regions. Considering these bipolar regions as a lower boundary, we extrapolate their field lines up to a height of 200 HMI pixels (72 Mm). For this purpose, we use the linear force-free extrapolation code, `j_b_lff.pro` (Nakagawa & Raadu 1972; Seehafer 1978), available within the SSW by setting the force-free parameter $\alpha = 0$. The field is therefore a potential field. Using the three-dimensional extrapolated magnetic fields data, we trace field lines through the volume corresponding to the XBP, following the streamline tracing method. For the streamline tracing, we have chosen the seed points (through which field lines pass) randomly within the extrapolated volume.

We assume that each traced field line corresponds to a coronal loop, and the loop has a constant radius (r) of 1 Mm throughout the height. The number of loops associated with an XBP is found by dividing the total area of the XBP in the masked AIA image by the combined cross-sectional area of the two footpoints. If the area of the ith XBP is A_i, then it contains N_i loops, where

$$N_i = \frac{A_i}{2\pi r^2}. \tag{2}$$

Using the coordinates (x_k, y_k, z_k) and magnetic field strength (B_{x_k}, B_{y_k}, B_{z_k}) of each of the loop along their length, we derive their length (L) and average magnetic field strength ($\langle B \rangle$) as follows:

$$L = \sum_k \sqrt{((x_{k+1} - x_k)^2 + (y_{k+1} - y_i)^2 + (z_{k+1} - z_k)^2)} \tag{3}$$

$$\langle B \rangle = \frac{\sum_k \sqrt{B_{x_k}^2 + B_{y_k}^2 + B_{z_k}^2} \times dl_k}{\sum_k dl_k}. \tag{4}$$

Figure 6 shows the AIA 193 Å image of one of the XBP in panel (a) and the corresponding HMI magnetogram in panel (b). Extrapolated field lines projected onto the plane of the sky are overplotted in blue, and a view of the magnetic skeleton from a different angle is shown in panel (c). The extrapolated field lines effectively capture the geometry of the XBP, as shown by a qualitative comparison between them and the brightening visible in the AIA image.

We find the existence of 25 XBPs inside the chosen area, F_v. For each of these XBPs, we extrapolate the magnetic field lines and estimate the loop lengths and magnetic field strengths. Figure 6(d) shows the distribution of all the loop lengths associated with all the XBPs, and Figure 6(e) shows the distribution of their average magnetic field strength ($\langle B \rangle$) along the loop length. The loop length distribution is found to peak near 30 Mm. The average magnetic field is found to vary inversely with loop length. The $\langle B \rangle \propto L^{-1}$ relation is overplotted by a black solid line as a reference.

4.2. Heating Function

Once the magnetic skeleton is created from the extrapolation, the loops need to be filled with heated plasma. We assume a spatially averaged volumetric heating function for each loop (erg cm^{-3} s^{-1}) that has two parts: impulsive heating by transient events (nanoflares) and steady background heating. The background heating is chosen such that it can maintain a temperature of approximately 5.0×10^5 K. The required heating rate can be estimated with a static equilibrium loop scaling law (Aschwanden 2005):

$$H_{bkg}[\text{erg cm}^{-3}\text{ s}^{-1}] \simeq \frac{2}{7}\left(\frac{10}{9}\right)^{\frac{7}{2}} k_0 \frac{\bar{T}^{\frac{7}{2}}}{L^2}. \tag{5}$$

Here, $k_0 = 8.12 \times 10^{-7}$ in cgs, and $\bar{T}$ is the average temperature (in our case 5.0×10^5 K) of the coronal part of the loop, which is related to the loop top temperature (T_a) as $\bar{T} \approx 0.9 T_a$ (Cargill et al. 2012).

Following Parker (1988) and Klimchuk (2015), an impulsive event can occur with the release of stored magnetic energy that derives from slow photospheric driving. If θ is the angle between the stress component and potential component of the field, then the density of free magnetic energy available for heating is

$$E = \frac{(\tan(\theta)\langle B \rangle)^2}{8\pi} (\text{erg cm}^{-3}). \tag{6}$$

In the picture of tangled and twisted magnetic strands, θ is the tilt of the magnetic field from vertical at the base of the corona. It is sometimes referred to as the *Parker angle*. It also corresponds to the misalignment half-angle between adjacent strands at the time they start to reconnect. To satisfy the observed coronal heating energy requirements, $tan(\theta) = c$ should be in the range of 0.2–0.3 (Parker 1988; Klimchuk 2015).

Following Klimchuk et al. (2008), Cargill et al. (2012), and Barnes et al. (2016), we define the impulsive heating function in terms of a series of symmetric triangular heating profiles having a duration (τ) of 100 s. The peak heating rate during an event (H_0) is randomly chosen between minimum ($H_0^{\min}$) and maximum ($H_0^{\max}$) values that are loop-dependent. $H_0^{\max}$ is determined from Equation (6), so for the jth loop of the ith XBP, it will be

$$H_{0_{ij}}^{\max} = \frac{1}{\tau}\frac{(c\langle B \rangle_{ij})^2}{8\pi} (\text{erg cm}^{-3}\text{ s}^{-1}). \tag{7}$$

$H_0^{\min}$ is taken to be $0.01 \times H_0^{\max}$.

As the free energy associated with a stressed loop is being released during an impulsive event, it is natural that releasing a larger amount of energy causes a larger delay in storing enough energy to be released during the next impulsive event. Taking into account this important consequence, we assume that the delay time between the two consecutive events is proportional to the energy of first event, i.e., the delay time between the

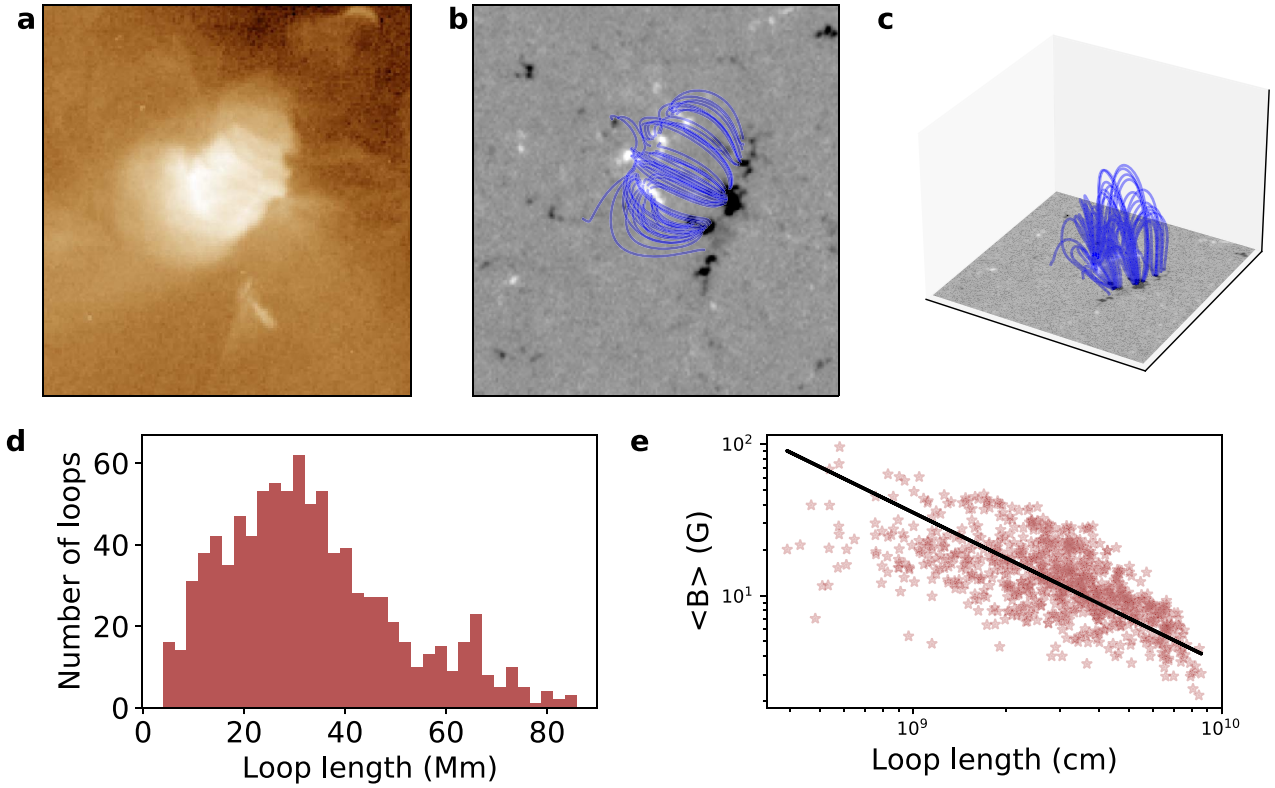

Figure 6. Panel (a) shows the representative image of an XBP as observed by AIA 193 Å channel. Panel (b) shows the HMI magnetogram associated with the XBP, and the blue curves are the plane-of-sky projected extrapolated field lines. A 3D view of the extrapolated field lines is shown in panel (c). Panels (d) and (e) show the distribution of the loop lengths and the magnetic field strength for all the loops associated with all the XBPs.

$(l-1)$th and lth event will be

$$d_{ij}^{l} = q \times H_{ij}^{l-1}. \tag{8}$$

The value of the proportionality constant, q, is estimated by equating the average Poynting flux (F in units of erg cm^{-2} s^{-1}) associated with a loop with the average energy released by the impulsive events. This makes the above equation in the form:

$$d_{ij}^{l} = \frac{\tau L}{F} \times H_{ij}^{l-1}. \tag{9}$$

In the present study, we estimate F by two different methods. The first method (called the Constant $-$ F model) assumes that all the loops associated with all the XBPs have the same average Poynting flux, which is calculated from the observed $\mathrm{DEM_{XBP}}$, as discussed in Section 4.2.1. The second method (called the Variable $-$ F model) assumes a different Poynting flux for each loop as discussed in Section 4.2.2.

4.2.1. Constant Poynting Flux (Constant–F Model)

The total radiation loss rate ($\mathcal{R}$) from the solar atmosphere can be estimated using the observed line-of-sight EMD (in units of cm^{-5}) and radiation loss function ($\Lambda(T)$) as follows:

$$\mathcal{R} = \sum_{i} \mathrm{EMD}(T_i)\Lambda(T_i). \tag{10}$$

Using the radiation loss function adopted in EBTEL (Klimchuk et al. 2008) and the observed EMD of the XBPs, we find that the average radiation loss for XBPs is 1.95×10^5 erg cm^{-2} s^{-1}.

The corona is cooled by both radiation and thermal conduction, with the latter providing the energy that powers the radiation from the transition region. The heating Poynting flux must therefore balance the total radiative losses, including those from the transition region. The computed EMD in Equation (10) does not extend below $\log T = 5.6$, because the cooler values cannot be reliably measured. We must account for this missing radiation. In equilibrium loops, the radiative losses from the transition region are larger than those from the corona, and these losses are greatest in the lower and middle transition region. Following Klimchuk et al. (2008), we take the total radiative losses in the loop to be 2–3 times larger than the coronal losses. Thus, the average Poynting flux to each loop is

$$F = g \times 1.95 \times 10^5 (\mathrm{erg\ cm^{-2}\ s^{-1}}), \tag{11}$$

where g is a constant in the range of 2–3.

Deriving the heating profile by combining Equations (7), (9), and (11) (Constant$-F$ model) has four variable parameters: L, $\langle B \rangle$, $c = \tan(\theta)$, and g. Figure 7(a) (blue line) shows the heating profile for a loop of $L = 30$ Mm, $\langle B \rangle = 10$ G, $g = 2.0$, and $c = 0.25$. The values of L and B are derived from the magnetic modeling of the photospheric magnetogram (Section 4.1), while the exact values of c and g are unknown. However, we know their expected range for the coronal loops as summarized in the first row of Table 1. We have varied the values of c and g within their expected range to match the observation as discussed in Section 4.3. Figure 7(b) shows the distribution of the heating events associated with the loop

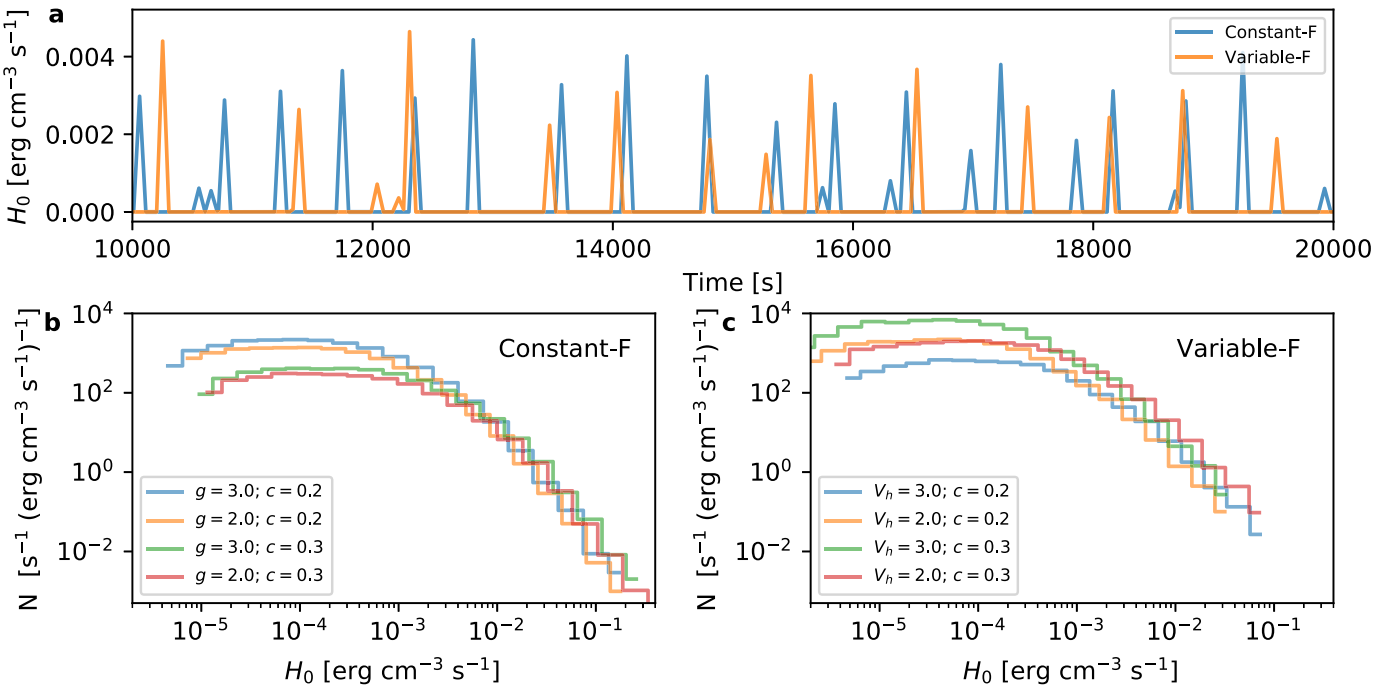

Figure 7. Panel (a) shows the representative heating function for a typical loop derived by using Constant−F and Variable−F models. Panels (b) and (c) show the heating frequency distribution of the events for the Constant−F and Variable−F models, respectively.

distribution of XBPs (Figure 6(d)) for the combination of $c = 0.2$, 0.3 and $g = 2.0$, 3.0.

4.2.2. Variable Poynting Flux (Variable−F Model)

It is to be noted that, even if the photospheric driver flows are the same, loops may not experience the same Poynting flux. This is because the field strengths vary from one loop to another. Following Klimchuk (2006), the expression for Poynting flux of individual loop can be written as

$$F = -\frac{1}{4\pi} V_h \tan(\theta)(\langle B \rangle)^2. \quad (12)$$

In this particular case, we have considered the loop to be nonexpanding, so that the field strength at the base of the corona is equal to the average field strength along the loop, $\langle B \rangle$. V_h is to be the horizontal speed of the flow that drives the field. However, this will not be the case if the loop expands with height. In such a situation, the cross-sectional area over which the Poynting flux energy enters the loop is smaller than the area over which it heats the plasma. We can account for this difference with the modified expression (see Appendix B)

$$F_{ij} = -\frac{1}{4\pi} V_h \tan(\theta) B_{ij}^{\rm base} \langle B \rangle_{ij}, \quad (13)$$

where $B^{\rm base}$ is the magnetic field at the coronal base and the subscripts refer to the jth loop of ith XBP. We take the coronal base to be 2 Mm above the photosphere, and we determine field strength there from the extrapolation.

The heating profile of the Variable−F model is obtained by combining Equations (7), (9), and (13). It has five variable parameters: L, $\langle B \rangle$, $B^{\rm base}$, $c = \tan(\theta)$, and V_h. Figure 7(a) (orange color) shows the derived heating profile for a loop of $L = 30$ Mm, $\langle B \rangle = 10$ G, $B^{\rm base} = 15$ G, $V_h = 1$ km s^{-1}, and $c = 0.25$. The values of L, $\langle B \rangle$, and $B^{\rm base}$ are estimated from the magnetic modeling of the loops, whereas the exact values of V_h and c are unknown. However, the expected ranges for these two variables are known, and these are summarized in the second row of Table 1. For an example, Figure 7(c) shows the distribution of the heating events corresponding to the loop distribution of XBPs (Figure 6(d)) for a combination of $V_h = 0.5$, 1.5 and $c = 0.2$, 0.3. This distribution is found to vary slightly according to the values of V_h and c, and thus we have varied the values of V_h and c within their expected range to match the observation as discussed in Section 4.3.

Table 1
Variable Parameters and Their Expected Ranges for the Constant−F and Variable−F Models

Model	$c = \tan(\theta)$	g	V_h(Km s^{-1})
Constant − F	0.2–0.3	2–3	⋯
Variable − F	0.2–0.3	⋯	0.5–2.0

4.3. Simulated DEM

Once the loop lengths and heating profiles for all the loops associated with all the XBPs are available, we run the EBTEL for individual loops in a parallel computing environment of a machine on 32 cores. Thus, in the simulation setup, EBTEL is called multiple times, and each call is associated with a different loop. We simulate the evolution of the loops for a duration of 20,000 s. The estimated DEMs of the transition region and coronal portion of the loops are stored for the last 7200 s of simulation time, similar to the observed DEM exposure time. Combining the DEMs of all the loops, we estimate the composite simulated DEM for all the XBPs.

The simulation setup is run multiple times by varying the input parameters within their expected range (Table 1) for both the Constant−F (Section 4.2.1) and Variable−F (Section 4.2.2) models. We estimate the composite simulated DEM for each

Table 2
Best-suited Parameters for the Constant−F and Variable−F Models

Model	$c = \tan(\theta)$	g	V_h(km s^{-1})
Constant − F	0.21	2.47	⋯
Variable − F	0.21	⋯	1.5

run and compare it with the observed DEM (DEM_{XBP}). The input parameters for which the simulated DEM well-describes the observed DEM based on visual comparison are summarized in Table 2 and plotted in Figure 8 (brown and blue colors). The transition region and coronal portion of the simulated DEM are shown by dotted and dashed lines, respectively, whereas solid lines show the total DEM. Though both models predict emission at higher temperatures ($\log T > 6.0$) that is close to the observed emission, they both predict emission at lower temperatures ($\log T < 6.0$) that is ∼2–5 times too high. This low-temperature emission primarily comes from the transition region of the loops, which is poorly constrained by the AIA channels, as indicated by the larger error bars in the observed DEM. Thus, the recovered DEM at low temperature can underpredict the actual emission, as demonstrated by Hannah et al. (2008). To verify this scenario, we have predicted the AIA and XSM intensities from the simulated DEMs of the transition region and corona, and we have recovered their DEMs using the `HK_dem` method (Section 3.5) by considering a typical 20% uncertainty in the simulated intensities. We find that the recovered coronal emission from the simulated intensities ($\log T > 6.0$ in Figure 9) matches well with the observed DEM. However, the recovered transition region DEM ($\log T<6.0$) still shows emission 2–3 times higher than that of the observed DEM. Thus, the deviation of the simulated and observed DEMs at a lower temperature is not only because of the observational uncertainty; rather, it indicates that the simulated transition region predicts a larger emission than the observed one—possible explanations for this deviation are given in Section 5.

4.4. Inferred Frequency Distribution

Figure 10(a) shows the frequency distribution of the impulsive event peak heating rates (H_0) for the model parameters that give the best match between simulated and observed DEMs (Table 2). At higher temperatures, the distribution is close to a power law of slope −2.5, as indicated by the gray reference line. We convert the heating rate distribution for the Constant−F model (blue dashed line in Figure 10(a)) to an energy distribution by integrating over the event duration and multiplying by the loop volume. This is shown as a blue dashed line in Figure 10(b), which is compared with the frequency distribution of the quiet Sun microflares as observed by XSM (Vadawale et al. 2021a). During the minimum of solar cycle 24, these microflares are found to occur everywhere on the Sun outside the conventional AR, and most of them are associated with the XBPs. A comprehensive discussion of this is given in Section 5.

5. Discussion and Summary

In the present work, we utilize the full-disk observations of the Sun using AIA and XSM to derive the DEM of the disk-integrated Sun ($DEM_{FullSun}$), X-ray emitting region (DEM_{XER}), and X-ray bright points (DEM_{XBP}) during the minimum of

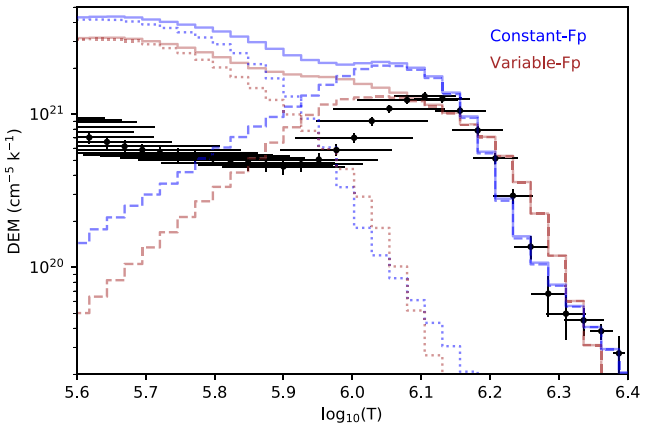

Figure 8. Observed DEM (black error bars) and DEMs simulated using the Constant−F (blue color) and Variable−F models (brown color). The contribution of the transition region and coronal DEMs to the total simulated DEM (solid lines) are shown separately by dotted and dashed lines.

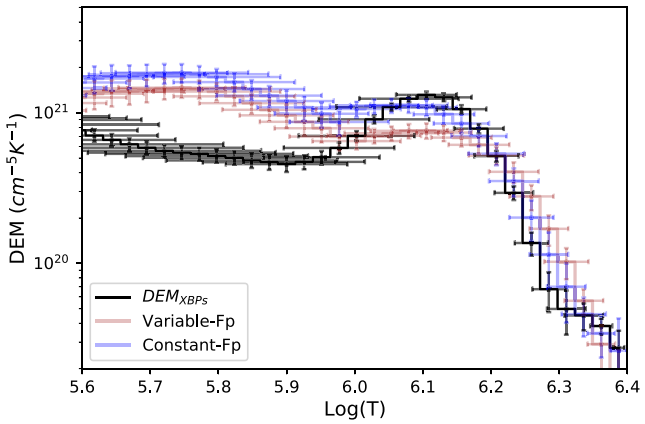

Figure 9. Observed DEMs of XBPs (black) compared with the recovered DEMs obtained from the simulated AIA and XSM intensities from the simulated DEM shown in Figure 8.

solar cycle 24. Our analysis suggests that, in the absence of ARs, XBPs are the primary contributor to the total X-ray emission of the full Sun. Using hydrodynamic loop simulations, we model the observed DEM of XBPs. The simulated DEM is then compared with the observed one. The primary findings of this paper are summarized below.

Quiet Sun coronal emission primarily consists of diffuse emission from the cool plasma and that of the XERs—The disk-integrated DEM ($DEM_{FullSun}$; Figure 2(a)) reveals a low-temperature (around 1 MK) peak along with an extended faint (approximately 2–3 orders of magnitude less than the peak around 1 MK) emission in the temperature range of $6.1 < \log(T) < 6.4$. The peak is likely to be dominated by the emission from the cool quiet region (also known as the diffuse corona) that occupies most of the solar disk. This peak emission is similar to earlier observations of the quiet Sun DEM (e.g., Lanzafame et al. 2005; Brooks et al. 2009; Del Zanna 2019; Sylwester et al. 2019). On the other hand, the extended faint but high-temperature ($\log T > 6.1$) emission is expected to be dominated by the X-ray emitting regions (XER). Using the full-disk images of AIA and corresponding observations from the XSM, we derive (Section 3.2) the DEM of XERs (DEM_{XER}; Figure 2(b)). Successively, the EMD of the same is also derived. A comparison between the EMD of

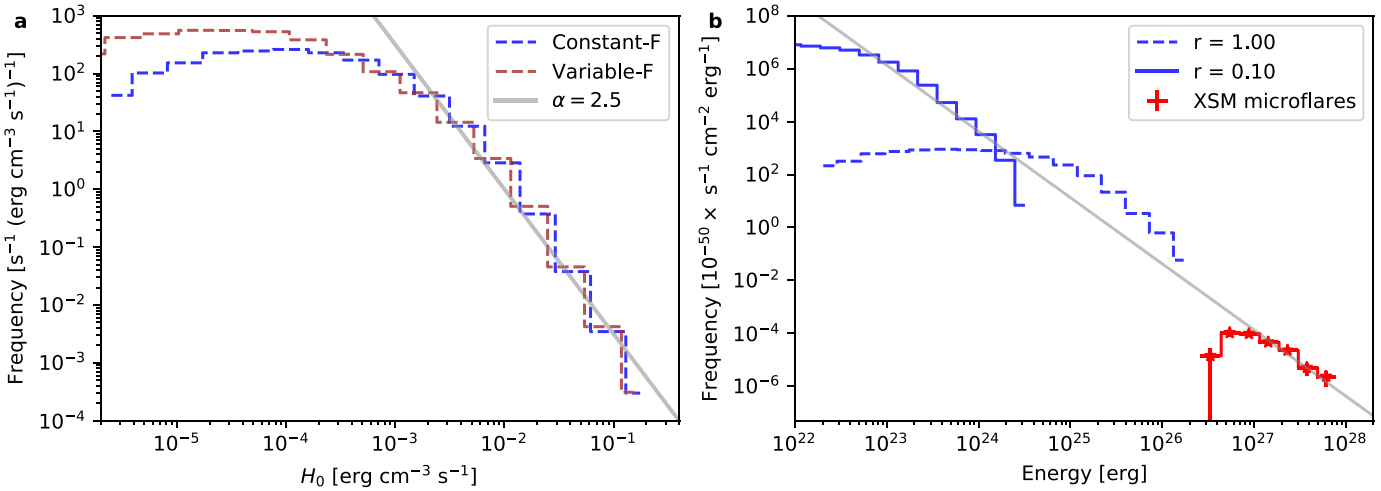

Figure 10. Panel (a) Heating frequency distribution of Constant−F (blue) and Variable−F (brown) models. Gray line represents a comparison power law with a slope of −2.5. Panel (b) Energy distribution of the events for the Constant−F model derived from the heating frequency shown in panel (a). The dashed and solid blue lines represent the energy distributions estimated by considering respective constant loop radii of 1 Mm and 0.1 Mm. The gray solid line represents the power-law function of slope −2.5, which intersects with the XSM observed microflare frequency distribution at higher energies.

the full Sun (Figure 2(c)) with that of the XERs (Figure 2(d)) shows that the high-temperature components are similar, indicating that the high-temperature emission of the full Sun is the primary source of the XERs.

During the quiet phase of the Sun, XBPs dominate the high-temperature emission observed by XSM—Figure 3 shows that, in the absence of on-disk ARs, the emissions from the limb and XBPs constitute most of the emissions of XERs. It is expected that limb brightening is primarily due to the emission coming from a large volume of low-temperature plasma. To distinguish the emission of XBPs from that of the overall XERs, we specifically derive (Section 3.3) the DEM of XBPs that are present at the center of the solar disk (Figure 5(a), blue color). DEM_{XER} and DEM_{XBP} display similar emissions when $\log(T) > 6.1$, indicating that, at this temperature range, XBPs primarily dominate the overall emission of XERs. In contrast, at low temperatures ($\log(T) < 6.1$), DEM_{XER} shows higher emission compared to DEM_{XBP}, which may be due to the contribution from the limb brightening in DEM_{XER}. For further verification, a typical DEM of the limb is derived from the intensity of a small limb area selected from the full-disk images taken by AIA and XRT (orange color in Figure 5). The limb DEM shows significant emission at low temperatures in the range $\log(T) < 6.1$.

To quantify the emission coming from the quiet regions, XER, and XBPs, radiative fluxes from each of these regions are estimated. Equation (10) is used for these estimations, while the inferred DEMs and the radiative loss function used in Klimchuk et al. (2008) are taken as input. Radiative fluxes are estimated in two temperature ranges; one is in the low-temperature emission ($\mathcal{R}(5.6 \leqslant \log T \leqslant 6.1)$) while the other is in the high-temperature emission ($\mathcal{R}(6.1 \leqslant \log T \leqslant 6.4)$) as is summarized in Table 3. The radiative flux of the full Sun, dominated by the quiet regions, is $\sim 0.9 \times 10^5$ erg cm^{-2} s^{-1}, which is close to the canonical quiet Sun value of Withbroe & Noyes (1977). The high-temperature component ($\log T > 6.1$) is almost an order of magnitude weaker than the cooler component. XBPs account for the 63% of the XER radiative flux at low temperatures ($\log T < 6.1$), while they contribute 85% at high temperatures (log(T) > 6.1). This indicates that, at high temperatures, most of the X-ray emissions observed by the XSM originate from the XBPs.

Table 3
Estimated Radiative Fluxes for the Full Sun, XER, and XBPs

DEM used	$\mathcal{R}(5.6 \leqslant \log T \leqslant 6.1)$ (erg cm^{-2} s^{-1})	$\mathcal{R}(6.1 \leqslant \log T \leqslant 6.4)$ (erg cm^{-2} s^{-1})
$DEM_{FullSun}$	0.78×10^5	0.09×10^5
DEM_{XER}	1.69×10^5	1.01×10^5
DEM_{XBP}	1.08×10^5	0.87×10^5

Results of the simulated XBPs agree well with the earlier findings—Like active regions, XBPs consist of small-scale coronal loops (Madjarska 2019). XBPs are found to be associated with bipolar regions (e.g., Figure 6(b)) on the photospheric magnetograms. Potential field extrapolation of these magnetograms (Section 4.1) provides the loop structures (e.g., Figures 6(a)–(c))) along with their length and magnetic field strength. The composite distribution of loop lengths associated with all the XBPs (Figure 6(d)) shows a peak at around 30 Mm, which is much smaller than the typical loop lengths of the ARs (order of 10^2 Mm; Aschwanden 2005). The average field strength (Figure 6(e)) of the loops is found to vary inversely with length to a power close to −1 (black solid line in Figure 6(e)), which is similar to the power law derived for AR loops (Mandrini et al. 2000).

We used the EBTEL hydrodynamic model and observational constraints to simulate XBP loops (Section 4). The loops were heated impulsively based on loop parameters derived from the extrapolations and observationally based assumptions about the input Poynting flux (Section 7). Two assumptions were considered: an equal Poynting flux for all loops (Constant−F model; Section 4.2.1) and Poynting fluxes that are loop-dependent (Variable−F model; Section 4.2.2). Each of these models is associated with two unknown parameters (c, g or c, V_h) as summarized in Table 1. Varying these parameters within their expected range obtained from earlier studies, we predicted the composite DEM of XBPs from the simulation and compared it with the observed one. The input parameters that provide the best match are summarized in Table 2. For the Variable−F model, the Parker angle (θ) is found to be $\sim 12^0$,

which is close to the typical value of 10^0 for ARs (Klimchuk 2015). The horizontal driver velocity is found to be $\sim$1.5 km s^{-1}, which is close to the observable range. For the Constant$-F$ model, the total energy losses from the corona, including thermal conduction, are found to be 2.5 times the coronal radiative losses. This is also consistent with expectations based on 1D hydrodynamic simulations.

Simulated DEM agrees well with the observed one at high temperatures—Figure 8 shows a comparison between the observed and simulated DEMs. The DEM obtained through the Constant$-F$ model (blue line) agrees well with the observed DEM (black error bars) at high temperatures ($\log(T) > 6.1$), where most of the emission comes from the corona (dashed blue line). The Variable$-F$ model (brown line), on the other hand, slightly overpredicts the DEMs at high temperatures. However, given the simplicity of the model, the differences of less than a factor of two are not significant.

The DEM is overpredicted by factors of two to five at low temperatures. This may be an artifact because of the instrument's broad temperature response functions. Such an artifact is expected to impact the observationally inferred DEM but not the simulated one. To check this, first we produce synthetic AIA and XSM intensities using the simulated DEM. These synthetic intensities are then further utilized to reconstruct a new DEM, as is done in case of actual observations (Figure 9). Though the discrepancy is reduced to a factor of two to three, the newly obtained DEM still shows high emission at low temperatures. Predicting excess emission at transition region temperatures ($\log T < 6.0$) is fairly common (e.g., Warren et al. 2008) in loop simulations. It must be mentioned that frequent chromospheric jets (such as spicules) are responsible for absorbing a significant amount (a factor of 2–3) of transition region emission (De Pontieu et al. 2009), causing a lower emission in the corresponding temperatures. Another possibility is that the emitting area of the transition region is reduced because loops are substantially constricted at their base due to the clumpiness of the magnetic field in the photosphere and the rapid transition from high-β to low-β conditions (Warren et al. 2010; Cargill et al. 2022).

Steep power-law slope for the nanoflares—When the heating rate is high, i.e., $H_0 > 10^{-3}$ erg cm^{-3} s^{-1}, the composite frequency distribution of all the loops maintains a power-law slope close to -2.5 (Figure 10(a)). Such a slope indicates that the combined energy of small-scale impulsive events or nanoflares are more than their larger counterparts, namely flares (Parker 1988) and microflares. Earlier observations also suggest (Vadawale et al. 2021a) that, in the quiet Sun, the larger events occur only occasionally, with an average frequency of $\sim$1.8 day^{-1}. The composite frequency distribution becomes flatter toward the lower heating rate (H_0).

Integrating the heating distribution (Figure 10(a)) over the duration of the event and multiplying by the loop volume, we obtain the typical flare energy distribution, shown by the dashed blue line in Figure 10(b). Extrapolating the distribution to higher energies disagrees with the earlier quiet Sun microflare distribution (red points) observed by XSM (Vadawale et al. 2021a). We also note that there is an excess of nanoflares at the lower energies. Our XBP models assume that loops have a radius of 1 Mm. Had we assumed a smaller radius of, say, 0.1 Mm, the energy per nanoflare would be reduced by a factor of 100 and there would be 100 times more loops in each XBP. The net effect is to shift the energy distribution to the left and upward, as shown by the solid blue curve in the figure. Now the nanoflares and microflares are closely explained by a single power-law distribution. We note that a coronal radius of 0.1 Mm is consistent with the expected size of elemental magnetic strands (Klimchuk 2015).

The slope of -2.5 obtained for the nanoflare frequency distribution is comparable to the frequency distribution reported in previous investigations (see, e.g., Benz & Krucker 2002; Purkhart & Veronig 2022) from the EUV brightenings in the quiet Sun. However, the slopes of these EUV observations vary significantly; for example, Purkhart & Veronig (2022) obtained a value of -2.02 to -2.47, Parnell & Jupp (2000) found -2.0 to -2.1, and Benz & Krucker (2002) found -2.3, whereas Aschwanden et al. (2000) and Joulin et al. (2016) found lower values of less than -2.0. It should be noted that the frequency distributions of nanoflares identified from the EUV observations are estimated with different biases and selection effects for the fundamental assumptions on various parameters (e.g., filling factor, plasma volume) during energy estimates. In contrast, our observations do not make such assumptions; instead, they depend on the loop parameters extrapolated from the observed photospheric magnetograms (see Section 4.2). It should also be noted that many studies have been concerned with small spatial scale, individually detected brightenings, presumably associated with tiny bipoles. The nanoflares that we model occur in longer loops and are not individually detected.

Carrying out a prolonged investigation of the quiet solar corona by separating out the contributions from its various emission components often becomes challenging in the Sun-as-a-star mode observations. Such an opportunity was provided by excellent observations of the quiet solar corona in the absence of any AR during the minimum of solar cycle 24. Estimating the DEM and subsequently the radiation flux of the quiet corona, X-ray emitting regions, and XBPs, we found most of the quiet or diffuse corona to emit at low temperatures ($\log T < 6.1$). In contrast, most emissions above $\log T = 6.1$ originate from XBPs. The DEM of the modeled XBPs indicates that XBP heating is likely to be maintained by the small-scale nanoflares. They originate through the release of stored magnetic energy within the stressed magnetic loops. Along with the sophisticated modeling efforts, spatially resolved spectroscopic observations with an instrument capable of both low- and high-temperature diagnostics are essential for comprehending the heating of small-scale loops. An imaging spectroscopic instrument with good spatial and energy resolution in the X-ray energy range (e.g., below 1 keV to 15 keV) could be beneficial in this context.

We acknowledge the use of data from the Solar X-ray Monitor (XSM) on board the Chandrayaan-2 mission of the Indian Space Research Organisation (ISRO), archived at the Indian Space Science Data Centre (ISSDC). The XSM was developed by Physical Research Laboratory (PRL) with support from various ISRO centers. We thank various facilities and the technical teams from all contributing institutes and the Chandrayaan-2 project, mission operations, and ground segment teams for their support. Research at PRL is supported by the Department of Space, Govt. of India. J.A.K. was supported by the Internal Scientist Funding Model (competed work package program) at Goddard Space Flight Center. We acknowledge support from the Royal Society through the

international exchanges grant No. IES\R2\170199. G.D.Z. and H.E.M. acknowledge support from STFC (UK) via the consolidated grant to the atomic astrophysics group at DAMTP, University of Cambridge (ST\T000481\1). B.M. acknowledges Dr. Sushree S. Nayak for the discussion of the magnetic field extrapolation. We are thankful to an anonymous referee for providing us with very useful feedback. A.B. was the J.C. Bose National Fellow during the period of this work.

Facilities: Chandrayaan-2(XSM), SDO(AIA, HMI), Hinode(XRT).

Appendix A
XSM and AIA Temperature Response

The XSM temperature responses are constructed from individual isothermal emission models over a logarithmic grid ($\delta(\mathrm{Log}T) = 0.03$) of temperatures ($T$) from 0.5 to 50 MK. We use the XSPEC (Arnaud et al. 1999) local model, `chisoth`[9] (Mondal et al. 2021), for the estimation of the isothermal emission spectrum at each temperature grid. As we are interested in the analysis of the quiet solar corona, we adopt the quiet Sun elemental abundances from Vadawale et al. (2021b). At the time of model calculation, we use the energy response (RMF) function of the XSM. However, because the XSM effective area varies with time, the time-varying effective area file (ARF) is used for the observation duration. These RMF and ARF are folded with the synthetic photon spectrum and produce the synthetic count spectrum of XSM in the units of counts s^{-1} keV^{-1} for an emission measure of 10^{46} cm^{-3}. We multiply the output spectrum by a factor (10^{-46} × energy bin), then further multiply by the emitting plasma area (e.g., the total area of X-ray emitting regions) to convert it into the units of counts cm^5 s^{-1} for a unit emission measure. To get the temperature response from these synthetic spectra at different temperature grids, we integrate the average counts over the dynamic energy bins of 1.29–1.45 keV, 1.45–1.75 keV, 1.72–1.95 keV, and 1.95–2.5 keV. Thus, we have a matrix of plasma temperatures and the XSM rebinned energy band for which we have the predicted count rates per unit emission measure.

The temperature response functions for the SDO/AIA EUV channels are obtained using the standard routine `aia_get_response.pro` available within the SSW. We use the same quiet Sun abundances obtained from Vadawale et al. (2021b) with CHIANTI version 10, and we adopted the latest calibrations, which incorporate the time-dependent corrections in the effective area. Figure A1 shows the temperature response functions for the AIA (dashed lines) channels along with the four XSM channels (solid lines) for integrated emissions of QS-1. It should be noted that the XSM temperature sensitivity starts to increase above 2 MK, whereas the AIA sensitivity starts dropping at those temperatures. Furthermore, XSM also shows a good overlap in temperature sensitivity with AIA. Thus, the combined DEM derived by XSM and AIA constrains both low- and high-temperature emissions.

Appendix B
Average Poynting Flux

It was argued earlier (Section 4.2.2) that, in the case of nonexpanding loops, one can evaluate the Poynting flux with Equation (12). However, this gets modified when we consider expanding loops. The Poynting flux at the base of the corona can be written as

$$F^{\mathrm{base}} = -\frac{1}{4\pi} V_h \tan(\theta)(B^{\mathrm{base}})^2. \tag{B1}$$

Here, B^{base} is the magnetic field strength at the base of the corona. Let us further consider A^{base} to be the area of the loop at the same location. If $\langle A \rangle$ and $\langle B \rangle$ are the average area and magnetic field strengths along the loop, respectively, then following the conservation of magnetic flux, one may write

$$B^{\mathrm{base}} A^{\mathrm{base}} = \langle B \rangle \langle A \rangle. \tag{B2}$$

Also, from the conservation of energy,

$$F^{\mathrm{base}} A^{\mathrm{base}} = HL \langle A \rangle, \tag{B3}$$

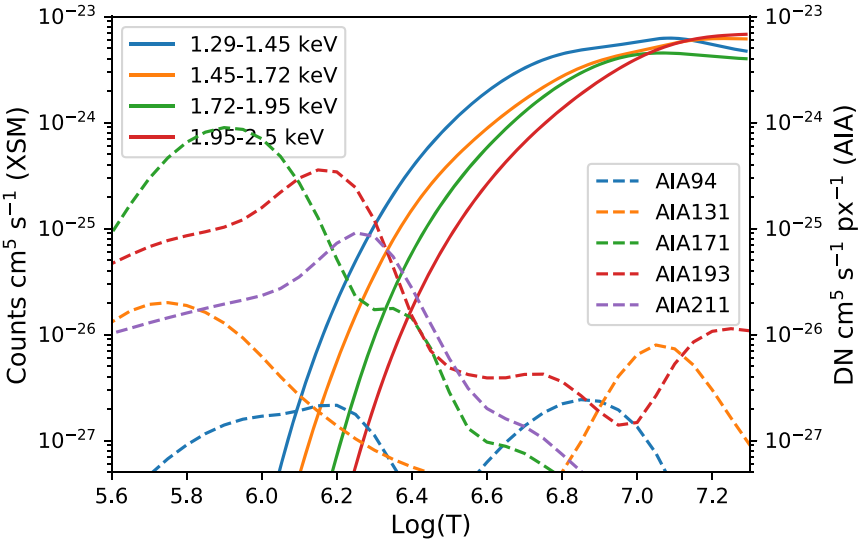

Figure A1. Temperature response functions for XSM (solid lines in units of Counts cm^5 s^{-1}) and AIA (dashed lines in units of DN cm^5 s^{-1} px^{-1}).

[9] https://github.com/xastprl/chspec

where H is the volumetric heating rate and L is the half-length of the loop. Combining Equations (B1), (B2), and (B3):

$$H = -\frac{1}{4\pi} V_h \tan(\theta) \frac{B^{\rm base} \langle B \rangle}{L}. \quad \text{(B4)}$$

This leads the expression for the Pointing flux of expanding loop to be

$$F = -\frac{1}{4\pi} V_h \tan(\theta) B^{\rm base} \langle B \rangle. \quad \text{(B5)}$$

ORCID iDs

Biswajit Mondal https://orcid.org/0000-0002-7020-2826
James A Klimchuk https://orcid.org/0000-0003-2255-0305
Santosh V. Vadawale https://orcid.org/0000-0002-2050-0913
Aveek Sarkar https://orcid.org/0000-0002-4781-5798
Giulio Del Zanna https://orcid.org/0000-0002-4125-0204
P. S. Athiray https://orcid.org/0000-0002-4454-147X
N. P. S. Mithun https://orcid.org/0000-0003-3431-6110
Helen E. Mason https://orcid.org/0000-0002-6418-7914
Anil Bhardwaj https://orcid.org/0000-0003-1693-453X

References

Arnaud, K., Dorman, B., & Gordon, C. 1999, XSPEC: An X-ray spectral fitting package, Astrophysics Source Code Library, ascl:9910.005
Aschwanden, M. J. 2005, in Physics of the Solar Corona. An Introduction with Problems and Solutions (2nd edition), ed. P. Blondel & J. Mason (Berlin: Springer Praxis)
Aschwanden, M. J., Tarbell, T. D., Nightingale, R. W., et al. 2000, ApJ, 535, 1047
Athiray, P. S., Vievering, J., Glesener, L., et al. 2020, ApJ, 891, 78
Barnes, W. T., Cargill, P. J., & Bradshaw, S. J. 2016, ApJ, 829, 31
Barnes, W. T., Cargill, P. J., & Bradshaw, S. J. 2016, ApJ, 833, 217
Benz, A. O., & Krucker, S. 2002, ApJ, 568, 413
Berghmans, D., Auchère, F., Long, D. M., et al. 2021, A&A, 656, L4
Boerner, P., Edwards, C., Lemen, J., et al. 2012, SoPh, 275, 41
Boerner, P. F., Testa, P., Warren, H., Weber, M. A., & Schrijver, C. J. 2014, SoPh, 289, 2377
Bradley, L., Sipőcz, B., Robitaille, T., et al. 2021, astropy/photutils: 1.2.0, Zenodo, doi:10.5281/zenodo.5525286, https://github.com/astropy/photutils
Bradshaw, S. J., & Viall, N. M. 2016, ApJ, 821, 63
Brooks, D. H., Warren, H. P., Williams, D. R., & Watanabe, T. 2009, ApJ, 705, 1522
Brosius, J. W., Daw, A. N., & Rabin, D. M. 2014, ApJ, 790, 112
Cargill, P. J., Bradshaw, S. J., & Klimchuk, J. A. 2012, ApJ, 752, 161
Cargill, P. J., Bradshaw, S. J., & Klimchuk, J. A. 2012, ApJ, 758, 5
Cargill, P. J., Bradshaw, S. J., Klimchuk, J. A., & Barnes, W. T. 2022, MNRAS, 509, 4420
Caspi, A., Woods, T. N., & Warren, H. P. 2015, ApJL, 802, L2
Chitta, L. P., Kariyappa, R., van Ballegooijen, A. A., et al. 2013, ApJ, 768, 32
Chitta, L. P., Peter, H., & Young, P. R. 2021, A&A, 647, A159
De Pontieu, B., Hansteen, V. H., McIntosh, S. W., & Patsourakos, S. 2009, ApJ, 702, 1016
Del Zanna, G. 2019, A&A, 624, A36
Del Zanna, G., & Mason, H. E. 2018, LRSP, 15, 5
Del Zanna, G., Tripathi, D., Mason, H., Subramanian, S., & O'Dwyer, B. 2015, A&A, 573, A104
Freeland, S. L., & Handy, B. N. 1998, SoPh, 182, 497
Golub, L., Deluca, E., Austin, G., et al. 2007, SoPh, 243, 63
Golub, L., Deluca, E. E., Sette, A., & Weber, M. 2004, in ASP Conf. Ser. 325, The Solar-B Mission and the Forefront of Solar Physics, ed. T. Sakurai & T. Sekii (San Francisco, CA: ASP), 217
Golub, L., Krieger, A. S., Silk, J. K., Timothy, A. F., & Vaiana, G. S. 1974, ApJL, 189, L93
Hannah, I. G., Christe, S., Krucker, S., et al. 2008, ApJ, 677, 704
Hannah, I. G., & Kontar, E. P. 2012, A&A, 539, A146
Ishikawa, S.-n., Glesener, L., Krucker, S., et al. 2017, NatAs, 1, 771
Joulin, V., Buchlin, E., Solomon, J., & Guennou, C. 2016, A&A, 591, A148
Katsukawa, Y., & Tsuneta, S. 2001, ApJ, 557, 343
Klimchuk, J. A. 2006, SoPh, 234, 41
Klimchuk, J. A. 2015, RSPTA, 373, 20140256
Klimchuk, J. A., Patsourakos, S., & Cargill, P. J. 2008, ApJ, 682, 1351
Kosugi, T., Matsuzaki, K., Sakao, T., et al. 2007, SoPh, 243, 3
Lanzafame, A. C., Brooks, D. H., & Lang, J. 2005, A&A, 432, 1063
Lemen, J. R., Title, A. M., Akin, D. J., et al. 2012, SoPh, 275, 17
Madjarska, M. S. 2019, LRSP, 16, 2
Mandrini, C. H., Démoulin, P., & Klimchuk, J. A. 2000, ApJ, 530, 999
Mithun, N. P. S., Vadawale, S. V., Sarkar, A., et al. 2020, SoPh, 295, 139
Mithun, N. P. S., Vadawale, S. V., Shanmugam, M., et al. 2021, ExA, 51, 33
Mondal, B., Sarkar, A., Vadawale, S. V., et al. 2021, ApJ, 920, 4
Nakagawa, Y., & Raadu, M. A. 1972, SoPh, 25, 127
Nita, G. M., Viall, N. M., Klimchuk, J. A., et al. 2018, ApJ, 853, 66
Parker, E. N. 1988, ApJ, 330, 474
Parnell, C. E., & Jupp, P. E. 2000, ApJ, 529, 554
Paterson, S., Hannah, I. G., Grefenstette, B. W., et al. 2022, arXiv:2210.01544
Pauluhn, A., & Solanki, S. K. 2007, A&A, 462, 311
Pesnell, W. D., Thompson, B. J., & Chamberlin, P. C. 2012, SoPh, 275, 3
Purkhart, S., & Veronig, A. M. 2022, A&A, 661, A149
Sakamoto, Y., Tsuneta, S., & Vekstein, G. 2008, ApJ, 689, 1421
Scherrer, P. H., Schou, J., Bush, R. I., et al. 2012, SoPh, 275, 207
Seehafer, N. 1978, SoPh, 58, 215
Shanmugam, M., Vadawale, S. V., Patel, A. R., et al. 2020, CSci, 118, 45
Sylwester, B., Sylwester, J., Siarkowski, M., et al. 2019, SoPh, 294, 176
Tripathi, D., Klimchuk, J. A., & Mason, H. E. 2011, ApJ, 740, 111
Vadawale, S., Shanmugam, M., Acharya, Y., et al. 2014, AdSpR, 54, 2021
Vadawale, S. V., Mithun, N. P. S., Mondal, B., et al. 2021a, ApJL, 912, L13
Vadawale, S. V., Mondal, B., Mithun, N. P. S., et al. 2021b, ApJL, 912, L12
Viall, N. M., & Klimchuk, J. A. 2012, ApJ, 753, 35
Viall, N. M., & Klimchuk, J. A. 2013, ApJ, 771, 115
Viall, N. M., & Klimchuk, J. A. 2015, ApJ, 799, 58
Warren, H. P., Winebarger, A. R., & Brooks, D. H. 2010, ApJ, 711, 228
Warren, H. P., Winebarger, A. R., Mariska, J. T., Doschek, G. A., & Hara, H. 2008, ApJ, 677, 1395
Winebarger, A. R., Schmelz, J. T., Warren, H. P., Saar, S. H., & Kashyap, V. L. 2011, ApJ, 740, 2
Withbroe, G. L., & Noyes, R. W. 1977, ARA&A, 15, 363
Wright, P., Hannah, I., Grefenstette, B., et al. 2017, ApJ, 844, 132